Chemical Engineering Journal 450 (2022) 137950

Contents lists available at ScienceDirect

Chemical Engineering Journal

journal homepage: www.elsevier.com/locate/cej

Sulfur-doped unsaturated Ni-N_3 coordination for efficient electroreduction of CO_2

Xian Yang [a], Jun Cheng [a,*], Hongkun Lv [b], Xiao Yang [a], Liwei Ding [b], Yang Xu [a], Kang Zhang [b], Weifu Sun [a], Junhu Zhou [a]

[a] State Key Laboratory of Clean Energy Utilization, Zhejiang University, Hangzhou 310027, China
[b] State Grid Zhejiang Electric Power Research Institute, Hangzhou 310014, China

ARTICLE INFO

Keywords:
CO_2 electroreduction
Single-atom catalyst
Coordination environment
density functional theory (DFT)

ABSTRACT

Tuning coordination environment of metal atoms in catalysts can improve intrinsic performance of CO_2 reduction and accelerate kinetics of CO formation. However, constructing unsaturated coordination configuration of metal single-atom by heteroatom doping still remains a challenge. Herein, a novel electrocatalyst of S/N co-coordinated Ni single-atom (denoted as Ni-SNC) was synthesized by calcining SO_4^{2-} doped Zn/Ni ZIF for electrocatalytic CO_2 reduction. The existence of single-atom Ni was verified by HAADF-STEM, while formation of "unsaturated" Ni-N_3-S active sites was confirmed by XANES and EXAFS. The energy barrier of pivotal steps in CO_2RR reaction process was reduced on "unsaturated" Ni-N_3-S active sites, and sulfur doping improved current density of electrocatalytic process. The energy barrier of CO_2→COOH* over Ni-SNC catalyst was only +0.69 eV, which was much less than that (+2.02 eV) over Ni-NC catalyst. The Ni-SNC exhibited CO Faradaic efficiency (FE_{CO}) of >90% at -0.6 ~ -0.9 V vs. RHE with the highest FE_{CO} of 95% at −0.8 V.

1. Introduction

Electrochemical CO_2 reduction (CO_2RR) into chemical energy employing intermittent renewable electricity is a promising technique [1,2]. However, the reaction mechanism is not only intensively competitive towards hydrogen evolution reaction (HER) but also has a high CO_2 activation energy barrier [3–6]. These factors make CO production more complicated and time-consuming. Noble metals catalysts (e.g., Au [7], Ag [8], and Pd [9]) are regarded as the most efficient catalysts due to their superior electroreduction of CO_2 to CO. However, the high cost and scarcity limit their widespread industrial application. Therefore, the development of an efficient non-noble metal electrocatalyst with excellent selectivity and superior current density is crucial.

Single-atom electrocatalysts have attracted considerable attention in the field of electrocatalysis in recent years [10]. Single-atom electrocatalysts performed better CO_2RR due to their highly unsaturated coordination environments, utilization of maximum atomic sites, and strong metal-substrate interactions [11]. Among these catalysts, Ni has higher CO_2 electroreduction activity and CO selectivity than Fe and Co [12]. In particular, Ni metal single atoms embedded in nitrogen-doped carbon substrates (Ni-NC) demonstrated exceptionally high faradaic efficiencies (FEs) (FE_{CO} > 90 %) for CO_2RR [13]. Regulating the coordination environment of single-atom active sites with precision to rationally design an efficient electrocatalyst is of great significance for boosting electrocatalytic reactions [14].

Furthermore, Ni-NC catalysts generally incorporate a range of Ni-N coordination environments, including Ni-N_4, Ni-N_3, and Ni-N_2 [15]. The Ni-N_4 coordination structure has remarkable electrocatalytic CO_2 reduction performance [12]. However, there are very few reports in the CO_2RR on unsaturated Ni-N_x coordination single-atom catalysts. Unsaturated Ni-Nx coordination has recently been investigated to substantially increase charge density distribution and intermediate CO* and COOH* adsorption energies of the Ni-N_4 coordination, as well as improve the ability of electrocatalytic reduction of CO_2 [16]. Nonetheless, this method is constrained by the precision with which unsaturated coordination environments are synthesized. Furthermore, unsaturated coordination can be obtained by doping heteroatoms such as S and P with weak electronegativity, which reduces the energy barrier of reaction intermediates [17]. The introduction of S and P atoms with larger atomic radius and lower electronegativity into the carbon skeleton can significantly tune the local electron density and thus significantly improve the activity and selectivity of single-atom catalysts. For

* Corresponding author at: State Key Laboratory of Clean Energy Utilization, Zhejiang University, Hangzhou 310027, China.
E-mail address: juncheng@zju.edu.cn (J. Cheng).

https://doi.org/10.1016/j.cej.2022.137950
Received 3 May 2022; Received in revised form 21 June 2022; Accepted 4 July 2022
Available online 8 July 2022

example, Zhao et al. demonstrated that introducing S can tune the local electronic density of unsaturated NiN_2 species, leading to improved CO_2RR performance at −0.8 V and −0.9 V vs RHE (FEco = 97%). Additionally, it was demonstrated that incorporation of the S enhanced the atomic local space available to foreign atoms for doping and reduced the CO* and COOH* energy barriers for CO_2RR to CO [18]. Li et al. also demonstrated that the incorporated sulfur engineered the charge on N atoms around the Fe reaction center [19]. Wang et al. introduced single P atoms into N-doped carbon-supported single iron atom catalysts (Fe-SAC/NPC), exhibited a CO Faradaic efficiency of 97% at a low overpotential of 320 mV. The presence of single P atoms increased the electron density of Fe center and stability of the key *COOH intermediate on Fe, leading to excellent CO_2RR performance at low overpotentials [20]. Apart from S and P heteroatoms, F atom doping can also be employed to tune the electronic configuration of Ni single-atoms, lowering the energy barrier for CO activation and favoring the formation of imperative intermediates COOH* [21]. However, doping heteroatoms required highly toxic chemicals like thiourea and PTFE, with moderate loading. Consequently, their remarkable electrocatalytic performance was significantly compromised. In this case, it is still challenging to develop a green and environmentally friendly method for preparing unsaturated coordination SACs with high loading and excellent stability for efficient electrocatalysis.

In this study, a new type SAC of S, N co-coordinated with Ni center embedded in three-dimensional carbon materials (denoted as Ni-SNC) is synthesized by calcining SO_4^{2-} doped Zn/Ni ZIF at 1000 °C in an argon atmosphere. The Ni-SNC demonstrated over 90% CO Faradaic efficiency (FE_{CO}) in the potential range of −0.6 to −0.9 V vs. RHE, with a peak FE_{CO} of 95% at −0.8 V vs. RHE in 0.5 M $KHCO_3$ electrolyte. The electronic structure of Ni single atom is adjusted by nitrogen and sulfur co-doping, making it a unique active site for CO_2 activation, according to both experimental and theoretical characterization results. The "unsaturated" coordination structure Ni-N_3-S has been revealed using X-ray absorption fine structure (XAFS). Furthermore, density functional theory (DFT) simulations demonstrate that unsaturated Ni-N sites and adjacent S atom groups improved local space charge separation, reducing the adsorption free energy of COOH* in the rate-limiting step, hence facilitating the electrocatalytic CO_2 reduction process.

2. Experimental

2.1. Materials

Carbon paper (TGP-H-060) was purchased from Toray Company. Nickel (II) nitrate hexahydrate ($Ni(NO_3)_2{\cdot}6H_2O$, 99%), Zinc (II) nitrate hexahydrate ($Zn(NO_3)_2{\cdot}6H_2O$, 99%), Zinc (II) sulfate heptahydrate ($ZnSO_4{\cdot}7H_2O$, 99%), and 2-methylimidazole were obtained from Macklin. Methanol (CH_3OH, for HPLC, >99.99%), sulfuric acid (H_2SO_4, 98%), and potassium bicarbonate ($KHCO_3$, 97%) were acquired from Shanghai Chemical Reagents, China. Nafion solution (10 wt%, D-520) and Nafion proton exchange membranes were utilized as received for catalyst ink preparation. All chemicals were used without additional purification.

2.2. Synthesis of the catalyst and preparation of the electrode

2.2.1. Synthesis of the Zn/Ni-ZIF, Zn-ZIF, S-Zn-ZIF, and S-Zn/Ni-ZIF catalysts

Firstly, 2.33 g $Zn(NO_3)_2{\cdot}6H_2O$ and 2.87 g $Ni(NO_3)_2{\cdot}6H_2O$ were added to 80 mL methanol under continuous stirring for ten minutes and the solution was labeled as solution A followed by dissolving 12.97 g 2-methylimidazole in another 80 mL methanol, and the resulting solution was marked as solution B. After that, solution B was quickly introduced to solution A. The final solution was kept stirring for 8 h at room temperature (25 °C) yielding the precipitates of catalyst. Finally, the product was centrifuged, washed multiple times with methanol and deionized water to remove impurities, and was subsequently dried in a vacuum oven for 12 h at 60 °C. The Zn/Ni-ZIF sample was obtained after drying.

Zn-ZIF was synthesized in the same way as Zn/Ni-ZIF but without the addition of $Ni(NO_3)_2{\cdot}6H_2O$. To synthesize S-Zn/Ni-ZIF, the same procedure as for Zn/Ni-ZIF was employed, except that 1.42 g $ZnSO_4{\cdot}7H_2O$ was introduced to the mixed A and B solutions after 4 h of stirring. The final solution was stirred continuously for another 4 h, yielding S-Zn/Ni-ZIF. S-Zn-ZIF was synthesized utilizing the same steps as for S-Zn/Ni-ZIF were followed, but without using $Ni(NO_3)_2{\cdot}6H_2O$.

2.2.2. Synthesis of the Ni-NC, NC, SNC, and Ni-SNC catalysts

To synthesize the Ni-SNC catalyst, a 0.8 g of dried S-Zn/Ni-ZIF sample was placed in a small quartz porcelain boat and pyrolyzed for 3 h at 1000 °C (5℃/min) in a tube furnace. For comparison, Ni-NC, NC, and SNC were also synthesized by following the same protocol as Ni-SNC, but with different precursors of Zn/Ni-ZIF, Zn-ZIF, and S-Zn-ZIF, respectively.

2.2.3. Preparation of the electrode

The catalyst ink was prepared by dispersing 5 mg of catalyst and 40 μL of Nafion solution (10 wt%) in 1 mL of ethanol followed by ultrasonication for 30 min. Then, using a pipette, 100 μL of catalyst ink was uniformly dropped on 1 cm × 1 cm^2 carbon paper. Finally, the catalyst-loaded carbon paper was dried for at least 30 min under infrared light.

2.3. Characterization

The X-ray diffraction (XRD) (Panalytical, Netherlands) with Cu-Kα radiation at 40 kV was performed to analyze the crystalline phase of the various catalysts. Scanning electron microscopy (SEM, FEI Quanta FEG 650, USA) and transmission electron microscopy (TEM, FEI TalosF200x, USA) were employed to examine the morphologies and microstructure. Single atoms were detected using high-angle annular dark field-scanning transmission electron microscopy (HAADF-STEM, JEOL, Japan). The chemical states of the catalyst surface were analyzed by X-ray photoelectron spectroscopy (XPS) using Al Kα radiation (Thermo Scientific, USA). The Micromeritics Tristar II3020 M has been utilized to analyze the pores size and specific surface area (BET) of a Ni single-atom catalyst. The Ni content of the Ni/NC and Ni/SNC catalysts were measured by an inductively coupled plasma spectrometer (Optima 7300 DV, USA). A Horiba HR800 spectrometer was employed to obtain Raman spectra. The Ni K-edge were recorded by X-ray absorption near-edge spectroscopy (XANES) and extended X-ray absorption fine structure (EXAFS) at BL14W beamline in Shanghai Synchrotron Radiation Facility (SSRF). The electron storage ring of SSRF was operated at 3.5 GeV with a maximum current of 250 mA. The data was recorded under fluorescence mode. Ni foil, NiPc, NiO, and Ni_3O_2 were used as the control samples.

2.4. Theoretical simulation method

DFT calculations were performed employing the Vienna Ab Initio Package (VASP) [22] by utilizing the PBE [23] formulation for the generalized gradient approximation (GGA). The projected augmented wave (PAW) potentials with plane-wave basis set and a kinetic energy cut-off of 400 eV were used to characterize the ionic cores [24] and to account for the valence electrons. Partial occupancies of the Kohn-Sham orbitals were allowed using the Gaussian smearing method and a width of 0.05 eV. When the energy change was less than 10^{-5} eV, it was deemed as self-consistent electronic energy. Geometry optimization was considered convergent when the force change was smaller than 0.02 eV/Å. Grimme's DFT-D3 methodology [25] was used to demonstrate the dispersion interactions.

The equilibrium lattice constant of hexagonal graphene monolayer unit cell separated by a vacuum layer in a depth of 15 Å was optimized to be a = 2.468 Å while using a 15 × 15 × 15 Monkhorst-Pack k-point grid for Brillouin zone sampling. It was then utilized to construct a graphene

monolayer surface model with p (6x6) periodicity in the × and y directions. This graphene model was comprised of 72C atoms. In this study, model 1 was doped with four N and one Ni atoms, while three N, one S, and one Ni atoms were doped in model 2. The gamma point in the Brillouin zone was employed for k-point sampling during structural optimizations, and all atoms were allowed to relax.

The free energy of a gas phase molecule or an adsorbate on the surface was calculated by the equation G = E + ZPE – TS.

where E is the total energy, ZPE is the zero-point energy, T is the temperature in kelvin (298.15 K), and S is the entropy.

2.5. CO_2 electrochemical reduction measurements

Electrochemical CO_2 reduction reaction (CO_2RR) characterizations were carried out in a typical three-electrode system connected to an electrochemical workstation (Ivium, Netherlands). A platinum wire was used as the counter electrode, Ag/AgCl was employed as the reference electrode, while the hydrophobic carbon paper supported catalyst was utilized as the working electrode. Both the cathode and anode were immersed in CO_2 saturated 0.5 M $KHCO_3$ electrolyte. High-purity CO_2 gas flowed continuously into the cathode cell (25 mL/min) during the electrochemical performance evaluation.

The gas products samples of CO and H_2 were collected online at a regular interval of 12 min using gas chromatography (GC, 7890 Agilent). All electrochemical experiments were performed in a three-compartment airtight glass cell. All the measured potentials were converted to hydrogen electrodes (RHE) according to the Nernst equation: $E_{RHE} = E_{Ag/AgCl} + 0.197 + 0.059 \times pH$.

3. Results and discussion

3.1. Characterization of the catalysts

Scheme 1 illustrates the synthesis of the Ni-SNC single-atom catalyst. At First, The S-Zn/Ni-ZIF was synthesized via in-situ doping of SO_4^{2-} into Zn/Ni-ZIF framework. The synthesized precursor S-Zn/Ni-ZIF was then calcined at 1000 °C in an Ar environment. Ni ions and surface SO_4^{2-} could be promptly transformed into Ni-SNC without the Ni-Ni agglomeration because of the spatial confinement effect of Zn nodes.

SEM and TEM have been employed to examine the morphologies of the catalysts, as shown in Fig. 1 (a-b). The regular dodecahedron morphology of the original ZIF precursor was still retained by Ni-SNC. After calcination, the sample's surface became rough and uniform in size, with an average diameter of approximately 100 nm. The incorporation of S sites may have resulted in the small size of Ni-SNC. The SEM images of ZIF-8, S-ZIF-8 and their carbonized samples are illustrated in Figure S1. In comparison to the original ZIF samples, SO_4^{2-} accelerated the nucleation of ZIF-8, leading to multiple regular dodecahedrons intercalating into each other, thereby smoothing the surface of S-ZIF-8 and drastically reducing its average size [26]. Aberration-corrected HAADF-STEM has been utilized to determine the existence of single atom Ni in the Ni-SNC catalyst, as demonstrated in Fig. 1 (c). The atomically dispersed Ni atoms in HAADF-STEM image of Ni-SNC are represented by multiple bright spots encircled by yellow circles. Fig. 1 (d-e) depict the EDS elemental mapping of the Ni-SNC, indicating that Ni, C, N, and S are dispersed uniformly throughout the Ni-SNC catalyst.

The XRD was used to further characterize the phase composition of the catalysts (Fig. 2 (a)). The results revealed that there was no peak for Ni crystals, however, two distinct diffraction characteristic peaks positioned at 24° and 44° corresponding to graphitic (002) and (100) planes respectively, were observed indicating that Ni in the form of single atoms is evenly disseminated in the catalyst rather than agglomerating into nanoparticles or other forms.

The specific surface area (BET) and pore size distribution of catalysts were measured by N_2 adsorption–desorption isotherms. The BET surface areas of the Ni-SNC, Ni-NC, NC, and SNC catalysts were 974.33, 656.88, 904.15, and 1017.79 m^2/g, respectively, as illustrated in Fig. 2 (b-c) and Table S1, while the average diameters of the Ni-SNC, Ni-NC, NC, and SNC catalysts were 3.13, 2.59, 1.91, and 2.05 nm. In particular, the nitrogen adsorption and desorption isotherms of Ni-SNC and SNC were consistent with Langmuir type I, type II, and hysteresis loops, implying the presence of both micropores and mesopores [27]. The adsorption volume reduced significantly in the low-pressure area, suggesting a reduction in the micropore region, however, it increased dramatically towards the tail of the isotherm (relatively high pressure), demonstrating the presence of a large number of mesopores [28]. The results revealed that sulfur doping caused pores enlargement, leading to composite pores/multiple porous structures comprised of mesopores and micropores, which significantly promoted mass transfer and CO diffusion (gas product), thereby improving CO_2RR efficiency. Fig. 2 (d) exhibits the Raman spectra of Ni-SNC and Ni-NC. Defects and disorders in the crystal structure are reflected by the D-band (~1350 cm^{-1}), whereas the G peak (~1580 cm^{-1}) is associated with the vibration of sp^2 carbon. The I_D/I_G values of Ni-NC and Ni-SNC catalysts were 1.02 and 1.07, respectively, [29] suggesting that Ni-SNC catalysts had more defects and disorders, offered more active sites, and had quicker surface mass transfer rate [30].

X-ray photoelectron spectroscopy (XPS) was utilized to investigate the elemental composition and chemical states of Ni SACs. As shown in Figure S3, the Ni-SNC catalyst sample is comprised of C, N, O, S, and Ni with no noticeable signal for Zn, implying that it had been completely evaporated during the calcination at 1000 °C. Meanwhile, Ni mass fraction in Ni-SNC was found to be 2.20% by inductively coupled plasma (ICP-MS). Fig. 3 (a) illustrates the high-resolution XPS Ni 2p spectra of

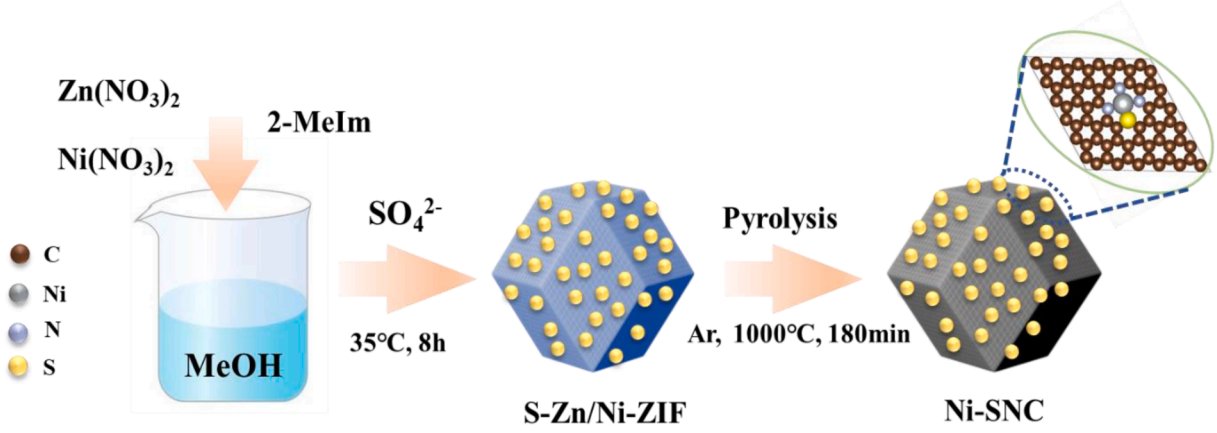

Scheme 1. Schematic for synthesis of Ni-SNC electrocatalyst.

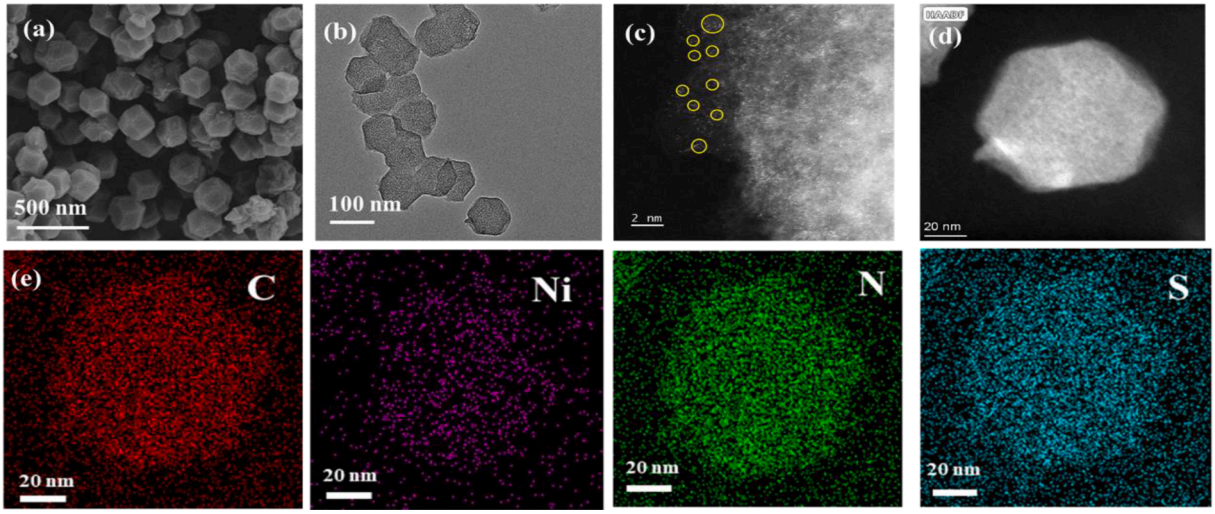

Fig. 1. (a) SEM, (b) TEM, and (c) HAADF-STEM images of Ni-SNC. (d-e) EDS elemental mapping images of Ni-SNC electrocatalyst.

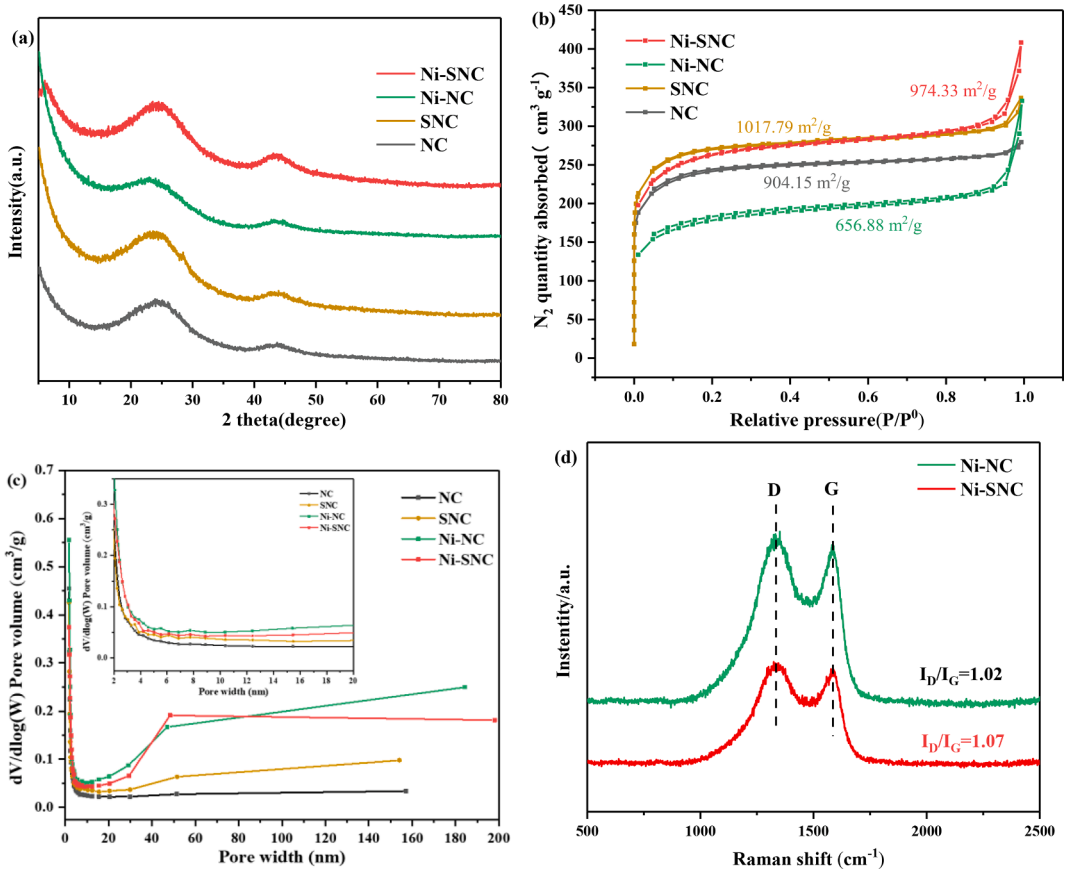

Fig. 2. (a) XRD patterns, (b-c) N_2 adsorption–desorption isotherms and corresponding pore size distribution of NC, SNC, Ni-NC, and Ni-SNC. (d) Raman spectra of Ni-NC and Ni-SNC.

Ni-NC and Ni-SNC. It is worth noting that the Ni $2p^{3/2}$ peak of Ni-NC and Ni-SNC was detected at binding energies of 854.18 eV and 854.55 eV, respectively. And the binding energies of Ni-NC and Ni-SNC catalysts were intermediate between that of Ni^{2+} (~856.0 eV) [31] and metallic Ni^0 (~852.9 eV) [32], showing that Ni SACs exhibited the valence state was located in the intermediate state $Ni^{\delta+}$ ($0 < \delta$ less than 2). Furthermore, as compared to Ni-NC, the Ni $2p^{3/2}$ and Ni $2p^{1/2}$ peaks in Ni-SNC shifted to higher binding energies (+0.37 eV), illustrating that the introduction of S might tune the coordination environment of single Ni atoms [33]. The high-resolution N 1 s spectra of Ni-NC and Ni-SNC were deconvoluted to five peaks positioned at 398.3, 398.9, 399.7, 401.3 eV, and 403.7 eV attributable to pyridinic N, Ni-N, pyrrolic N, graphitic N, and oxidized N, respectively, as shown in Fig. 3b. The pyridinic N content reduced from 29.9% to 17.1%, while the pyrrolic N content increased from 10.77% to 16.5%, as illustrated in Figure S4. This might be due to the doping S bonded to carbon atoms adjacent to the pyridinic nitrogen, converting the pyridinic nitrogen to pyrrolic nitrogen [34].The high-resolution S 2p spectra of SNC and Ni-SNC are displayed in Fig. 3

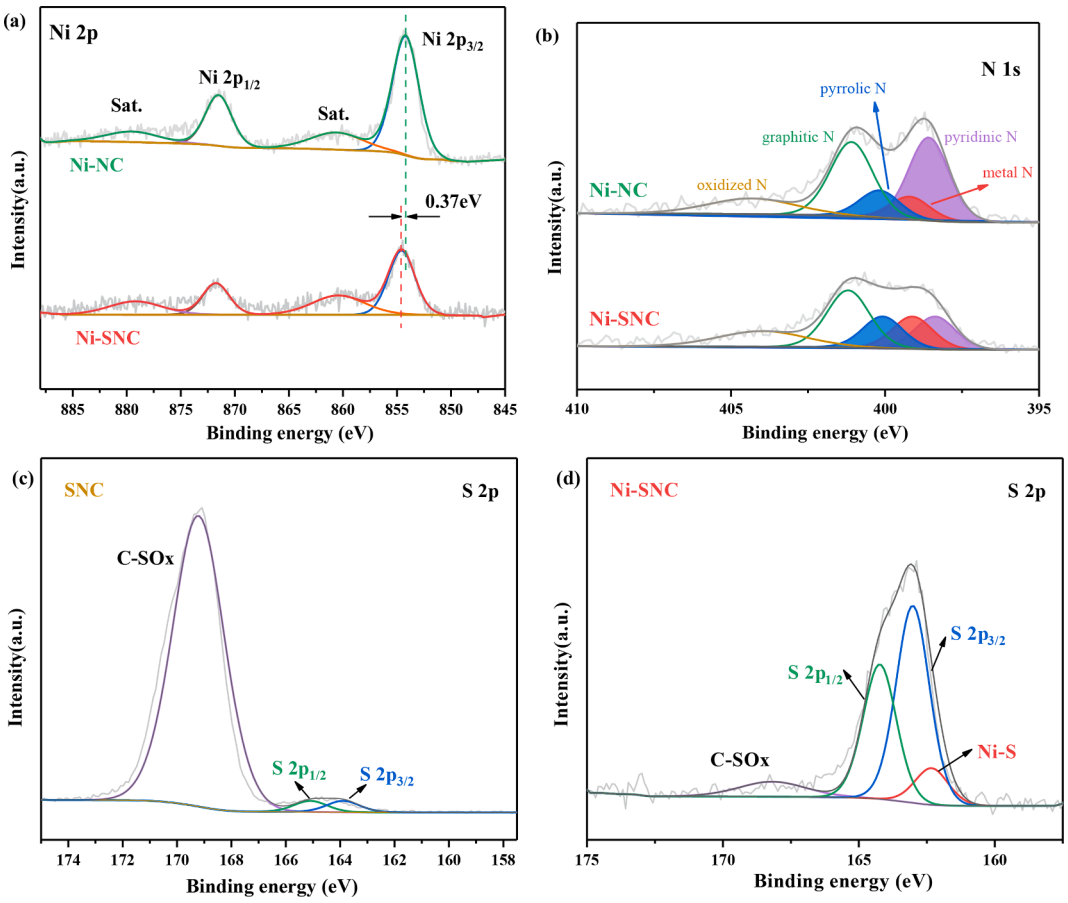

Fig. 3. (a) Ni 2p XPS spectra, (b) N 1 s XPS spectra of Ni-NC and Ni-SNC. (c-d) S 2p XPS spectra of SNC and Ni-SNC.

(c-d). The peaks corresponding to S $2p^{3/2}$ and S $2p^{1/2}$ are observed at 163.5 and 164.7 eV, respectively. Two of the peaks were ascribed to the C-S-C species [35], while the peaks at 170.2 eV were associated with C-SO_x species [36]. Compared to SNC, the proportion of C-SO_x reduced dramatically while the proportion of C-S-C increased after nickel doping, as demonstrated by the high-resolution S 2p spectrum of Ni-SNC. Interestingly, a small peak was also discovered at 162.7 eV, which might correspond to the Ni-S bond, emphasizing that S doping produced a coordination structure with Ni and modified the surface chemical state of Ni atoms concurrently [37]. The introduction of S atoms significantly tuned the local electron density of the central atom Ni and accelerated the activation of H_2O, providing enough protons to facilitate the conversion of CO_2 to *COOH. As shown in Figures S4, the C 1 s spectra of the Ni-SNC catalyst could be deconvoluted into three peaks: centered at 284.8 eV (C—C/C═C), 286.0 eV (C—N/C—S) and 289.9 eV (C═O), demonstrating that N species were successfully doped into the carbon matrix [38]. Deconvoluted high-resolution O 1 s XPS spectrum of the Ni-SNC displayed the peak centered at 530.6 eV, which could be assigned to the Ni-bonded O formation [39]. Ni-O coordination reduced the reaction barriers of CO_2* to COOH* as the limiting step, thus promoting the CO_2RR activity of Ni-SNC [40].

The detection of Ni K-edge by X-ray absorption near-edge spectroscopy (XANES) and extended X-ray absorption fine structure (EXAFS) were recorded to further elucidate the coordination structure of the core Ni atoms in the Ni-SNC, as shown in Fig. 4. When the normalized XANES spectra Ni-SNC were compared to those of reference materials, it was discovered that the near-edge adsorption energy of Ni-SNC lies between that of Ni foil and NiO, revealing that average valence state of Ni to be in between + 1 and + 2, as illustrated in Fig. 4a. These results further confirmed that sulfur doping impacted the coordination environment of central Ni atoms. The dominant peak of the Ni-SNC sample originated at 1.57 Å in the Fourier transformation of the EXAFS spectra (Fig. 4b), while there was no obvious Ni–Ni peak (2.15 Å), proving that Ni single atoms were uniformly distributed on the nitrogen-doped carbon substrate without agglomeration into Ni nanoparticles, which is consistent with the aberration-corrected HAADF-STEM. The peak positions of Ni-N and Ni-O were 1.47 Å and 1.65 Å, respectively as compared to the reference materials NiPc and NiO. The coordination of Ni-N altered with the introduction of S atoms, and the average length of the Ni-N bond increased. To further demonstrate the effect of S doping on the coordination environment of Ni central atoms, the FT-EXAFS fitting of Ni-SNC was performed in R and k space. All of the fitting results are consistent with the experimental data, as shown in Fig. 4(c-d). The average coordination number of the Ni-N (first shell) of Ni-SNC was calculated to be 2.9, with an average bond length of 1.89 Å. And the coordination number of the Ni-S (second shell) was 1.3 with an average bond length of 1.94 Å, as well as the coordination structure of Ni-N_3-S was found to be consistent with the coordination structure of Ni-SNC, as depicted in Table S3 [41].

3.2. *CO_2 electrocatalytic reduction*

A typical three-electrode system has been employed to evaluate the electrocatalytic performance of catalysts for CO_2RR in 0.5 M $KHCO_3$ solution saturated with Ar and CO_2. A gas chromatograph (GC) was utilized to identify the reaction's gas-phase product CO, while no liquid-phase product was detected. Fig. 5a depicts the linear sweep voltammetry (LSV) plots of NC, SNC, Ni-NC, and Ni-SNC. Notably, the Ni-SNC catalyst exhibited the highest current density while the current density of SNC was also higher than the NC catalyst, demonstrating that S doping could expedite the charge transfer in the catalyst for CO_2RR. Furthermore, Ni-SNC catalysts exhibited substantially higher current

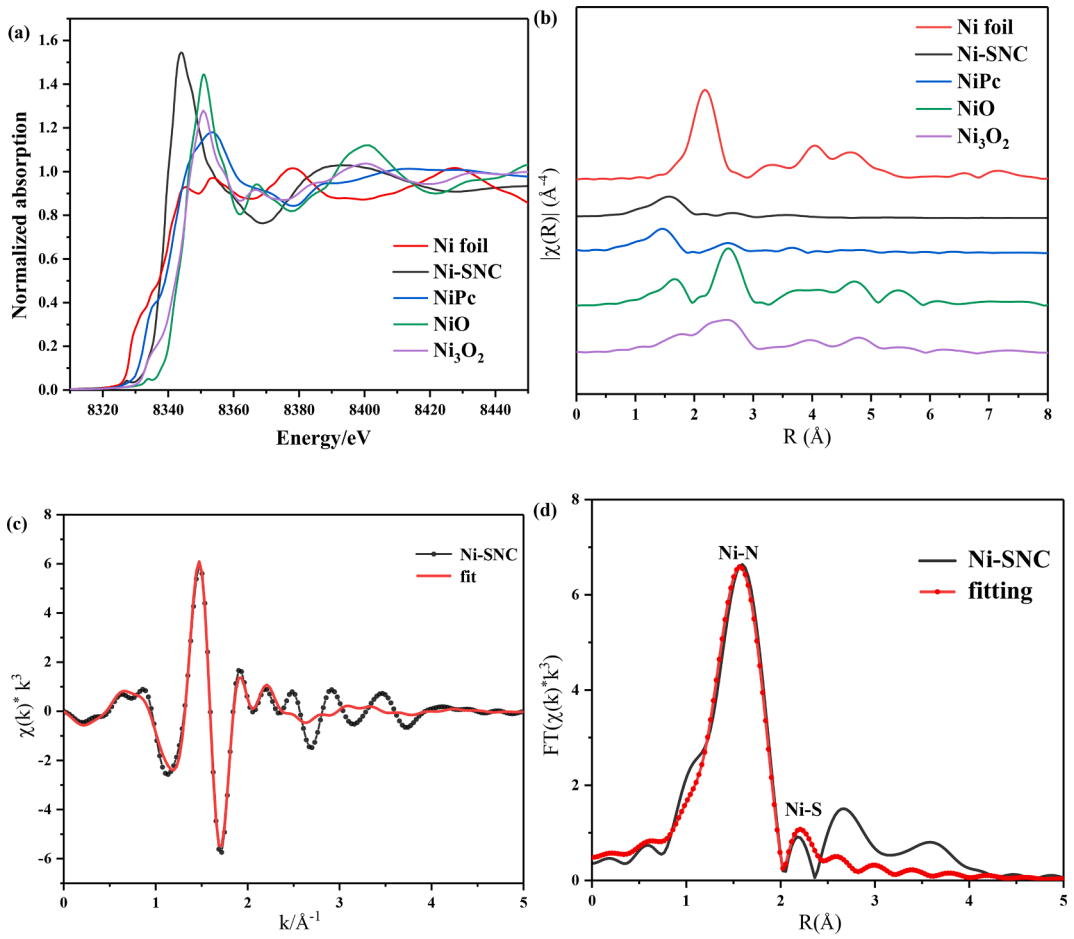

Fig. 4. (a) Ni K-edge XANES spectra, (b) FT-EXAFS spectra of Ni-SNC and the references (Ni foil, NiPc, NiO, and Ni_3O_2), (c-d) corresponding FT-EXAFS fitting curves of Ni-SNC catalyst.

density in CO_2-saturated electrolytes than Ar-saturated electrolytes, depicting that S doping can improve the activity and selectivity of the catalyst in CO_2RR. Catalyst samples were tested for CO_2RR performance at different potentials as indicated in Fig. 5(c-d). Remarkably, the FE_{CO} of the Ni-SNC was higher than that of NC, SNC, and Ni-NC over the entire potential range. Additionally, the Ni-SNC attained FE_{CO} of over 90% from −0.6 V to −0.9 V vs. RHE, with a maximum FE_{CO} of 95% at −0.8 V. In addition, the FE_{CO} of the SNC was greater than that of NC after S doping, especially in the low potential range. The CO partial current density (j_{CO}) was also determined. Ni-SNC had a substantially higher current density than the other samples. Furthermore, the current density of Ni-SNC reached 11 mA/cm^2 at −0.8 V, which was substantially higher than that of NC (1.3 mA/cm^2), SNC (3.66 mA/cm^2), and Ni-NC (4.72 mA/cm^2). According to these results, the introduction of S atoms to the Ni-N_x structure can significantly improve the activity and selectivity of CO_2RR while also tuning the coordination environment and charge distribution of the central Ni atom [42].

Furthermore, the inherent activity of the catalyst for CO_2RR was evaluated by electrochemical specific surface area (ECSA) analysis. The ECSA was calculated by scanning the CV at different scan rates in accordance with the double-layer capacitance (C_{dl}) theory, as illustrated in Figures S6 and S7. Ni-SNC exhibited the highest C_{dl} value of 56.2 mF cm^{-2} as compared with other samples: NC (4.5 mF cm^{-2}), SNC (10.6 mF cm^{-2}), and Ni-NC (21.2 mF cm^{-2}) indicating that Ni-SNC could expose more active sites. Electrochemical impedance spectroscopy (EIS) was utilized to study CO_2RR reaction kinetics. The charge transfer resistance (R_{ct}) of the Ni-SNC and Ni-NC catalysts was depicted in the corresponding Nyquist plots. The R_{ct} (8.2 Ω) of the Ni-SNC was lower than the R_{ct} of Ni-NC (18.5 Ω). The Smaller R_{ct} of Ni-SNC revealed faster reaction kinetics and electron transfer for CO_2RR than Ni-NC. In addition to excellent electrocatalytic activity for CO_2RR, Ni-SNC exhibited outstanding stability; during 24-hour continuous potentiostatic electrolysis at −0.8 V, the current density remained highly stable, while maintaining CO Faradaic efficiency above 90%. As shown in Figure S9, XRD patterns showed that there was no peak of Ni nanoparticles before and after CO_2 reduction reaction. We also compared XPS of Ni-SNC before and after CO_2 reduction. The main peaks of Ni 2p, N 1 s and S 2p spectra did not change significantly after CO_2RR, indicating that the catalyst has an excellent stability during CO_2 reduction. The results indicated that the structural stability of single-atom Ni-SNC catalyst.

3.3. *Theoretical calculations and catalytic mechanism*

In order to understand the improved CO_2RR performance of Ni-SNC, DFT simulations were performed, for which the Ni-N_3-S model was constructed based on the EXAFS fitting results. There are three stages to the electroreduction of CO_2 to CO, as shown in Fig. 6(a) according to previously reported studies. The adsorption of CO_2 to COOH* and the conversion of COOH* to CO* are the major rate-limiting steps for the reduction of CO_2 to CO on the catalyst surface. The CO_2 molecules first adsorb protons to generate *COOH, which is then converted to *CO, and finally *CO desorbed off the catalytic surface. The free energy of the reaction was calculated and displayed in Fig. 6(b). It can be seen that CO_2 (g) → COOH* is an endothermic reaction. The CO_2 to COOH* energy barrier of Ni-SNC was calculated to be only + 0.69 eV by DFT calculations, which was significantly lower than that of Ni-NC (+2.02

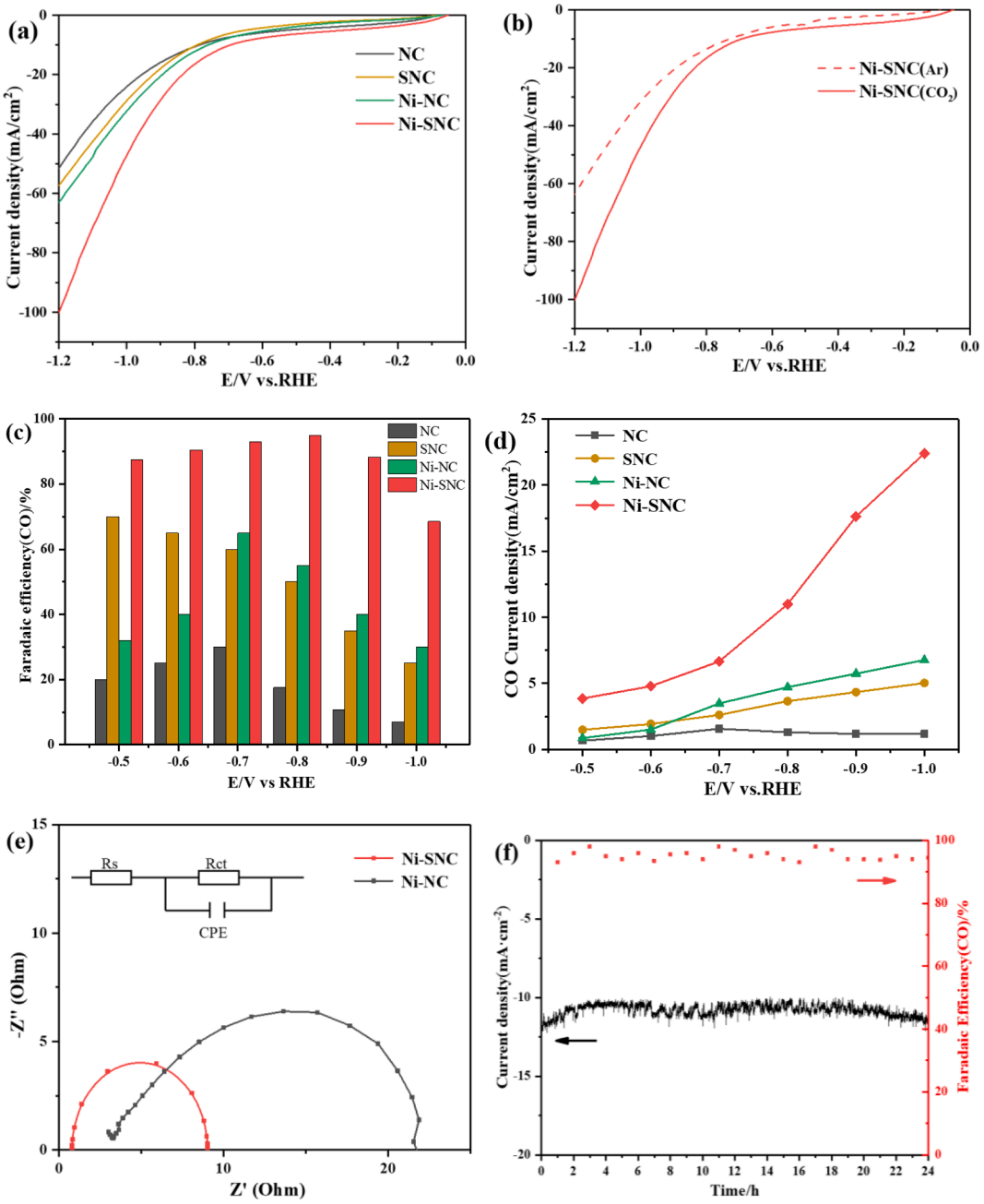

Fig. 5. (a) LSV curves of NC, SNC, Ni-NC, and Ni-SNC in CO_2-saturated 0.5 M $KHCO_3$. (b) LSV curves of Ni-SNC in Ar-saturated and CO_2-saturated 0.5 M $KHCO_3$. (c) FEs of CO over different catalysts. (d) CO partial current density. (e) Nyquist plots of Ni-NC and Ni-SNC. (f) Ni-SNC longterm stability test at −0.8 V vs. RHE for 24 h continuous potentiostatic electrolysis. The dots and solid line show FE_{CO} and corresponding current density, respectively.

eV). On the other hand, Ni-SNC exhibited a lower CO* adsorption energy (-0.167 eV) than that of Ni-NC (+0.963 eV). Activation of CO_2 by sulfur doping was shown to improve the formation of the intermediate COOH* while simultaneously reducing the adsorption of CO* on the catalyst surface, which is crucial for the desorption of CO* [43]. This suggested that the electrocatalytic conversion of CO_2 to CO was facilitated by the coordinatively unsaturated Ni-N structure generated by S doping. According to these results, Ni-N_3-S is more active and selective for CO_2RR to CO than Ni-N_4, which is completely consistent with the experimental results.

4. Conclusion

In summary, a novel and stable S-doped Ni SAC electrocatalyst have been developed for electrochemical reduction of CO_2 to CO. The existence of Ni single-atom and "unsaturated" Ni-N_3-S active sites was confirmed by HAADF-STEM and EXAFS. Ni-SNCs demonstrated excellent electrocatalytic activity and high CO selectivity due to the synergistic effect of doped S and atomically dispersed "unsaturated" Ni-N_3-S active sites. In particular, the Ni-SNC catalyst achieved a FE_{CO} of over 90% from −0.6 V to −0.9 V vs. RHE and the maximum FE_{CO} value reached 95% at −0.8 V. According to DFT simulations, the "unsaturated" Ni-N_3-S sites dominated mostly due to the appropriate binding energy strength of the intermediate species. In comparison to Ni-NC, Ni-SNC exhibited lower COOH* and CO* free energies, which might lower the reaction kinetic energy barrier of the rate-limiting step, improve CO desorption, and enhance the electrocatalytic CO_2 reduction. Briefly, this research opened up new avenues for modifying single-atom active sites,

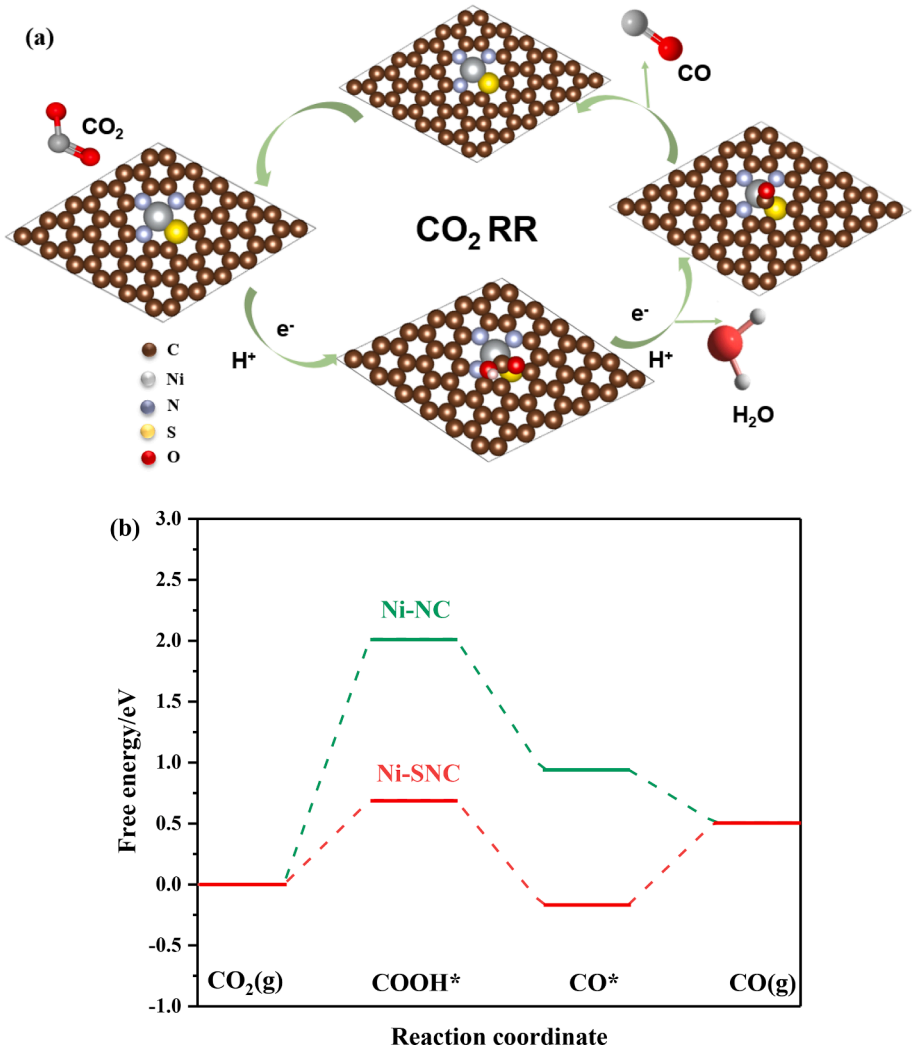

Fig. 6. (a) Schematic of CO_2RR on Ni-N_3-S active site. (b) Free energy diagram of Ni-NC and Ni-SNC catalysts for CO_2RR.

coordination environments, and fabricating developing unsaturated Ni-N coordination catalysts, as well as revealed the utilization of hetero-atoms (such as S, P, etc.) to improve electrocatalytic performance.

Declaration of Competing Interest

The authors declare that they have no known competing financial interests or personal relationships that could have appeared to influence the work reported in this paper.

Data availability

The authors do not have permission to share data.

Acknowledgements

The authors are grateful to financial support from State Grid Corporation of China under Project "Research and Application on Methanol Production, Storage and Utilization from Electrolytic CO_2 for Clean Alternative of Terminal Fuel" (Grant NO. 5400-202219176A-1-1-ZN).

Appendix A. Supplementary data

Supplementary data to this article can be found online at https://doi.org/10.1016/j.cej.2022.137950.

References

[1] W. Choi, M. Kim, B.-j. Kim, Y. Park, D.S. Han, M.R. Hoffmann, H. Park, Electrocatalytic arsenite oxidation in bicarbonate solutions combined with CO_2 reduction to formate, Appl. Catal. B 265 (2020) 118607.
[2] X. Xuan, M. Wang, M. Zhang, Y.V. Kaneti, X. Xu, X. Sun, Y. Yamauchi, Nanoarchitectonics of low-dimensional metal-organic frameworks toward photo/electrochemical CO_2 reduction reactions, J. CO_2 Util. 57 (2022) 101883.
[3] D.D. Zhu, J.L. Liu, S.Z. Qiao, Recent advances in inorganic heterogeneous electrocatalysts for reduction of carbon dioxide, Adv Mater 28 (18) (2016) 3423–3452.
[4] L. Zhang, Z.-J. Zhao, J. Gong, Nanostructured materials for heterogeneous electrocatalytic CO_2 reduction and their related reaction mechanisms, Angew Chem Int Ed Engl 56 (38) (2017) 11326–11353.
[5] S. Wang, P. Zhou, L. Zhou, F. Lv, Y. Sun, Q. Zhang, L. Gu, H. Yang, S. Guo, A unique gas-migration, trapping, and emitting strategy for high-loading single atomic Cd sites for carbon dioxide electroreduction, Nano Lett 21 (10) (2021) 4262–4269.
[6] W. Ni, Z. Liu, Y. Zhang, C. Ma, H. Deng, S. Zhang, S. Wang, Electroreduction of carbon dioxide driven by the intrinsic defects in the carbon plane of a single Fe-N4 site, Adv Mater 33 (2021) e2003238.
[7] Z. Cao, S.B. Zacate, X. Sun, J. Liu, E.M. Hale, W.P. Carson, S.B. Tyndall, J. Xu, X. Liu, X. Liu, C. Song, J.-H. Luo, M.-J. Cheng, X. Wen, W. Liu, Tuning gold nanoparticles with chelating ligands for highly efficient electrocatalytic CO_2 reduction, Angew Chem Int Ed Engl 57 (39) (2018) 12675–12679.
[8] S. Liu, X.-Z. Wang, H. Tao, T. Li, Q. Liu, Z. Xu, X.-Z. Fu, J.-L. Luo, Ultrathin 5-fold twinned sub-25 nm silver nanowires enable highly selective electroreduction of CO_2 to CO, Nano Energy 45 (2018) 456–462.
[9] D. Gao, H.u. Zhou, F. Cai, J. Wang, G. Wang, X. Bao, Pd-containing nanostructures for electrochemical CO_2 reduction reaction, ACS Catal. 8 (2) (2018) 1510–1519.
[10] Y.i. Cheng, S. Yang, S.P. Jiang, S. Wang, Supported single atoms as new class of catalysts for electrochemical reduction of carbon dioxide, Small Methods 3 (9) (2019) 1800440.

[11] W. Guo, X. Tan, J. Bi, L. Xu, D. Yang, C. Chen, Q. Zhu, J. Ma, A. Tayal, J. Ma, Y. Huang, X. Sun, S. Liu, B. Han, Atomic indium catalysts for switching CO_2 electroreduction products from formate to CO, J Am Chem Soc 143 (18) (2021) 6877–6885.
[12] W. Ju, A. Bagger, G.P. Hao, A.S. Varela, I. Sinev, V. Bon, B. Roldan Cuenya, S. Kaskel, J. Rossmeisl, P. Strasser, Understanding activity and selectivity of metal-nitrogen-doped carbon catalysts for electrochemical reduction of CO_2, Nat Commun 8 (2017) 944.
[13] X. Yang, J. Cheng, B. Fang, X. Xuan, N. Liu, X. Yang, J. Zhou, Single Ni atoms with higher positive charges induced by hydroxyls for electrocatalytic CO_2 reduction, Nanoscale 12 (35) (2020) 18437–18445.
[14] Y. Wang, X. Zheng, D. Wang, Design concept for electrocatalysts, Nano Res. 15 (3) (2022) 1730–1752.
[15] Y. Zhang, L. Jiao, W. Yang, C. Xie, H.-L. Jiang, Rational fabrication of low-coordinate single-atom Ni electrocatalysts by MOFs for highly selective CO_2 reduction, Angew Chem Int Ed Engl 60 (14) (2021) 7607–7611.
[16] C. Yan, H. Li, Y. Ye, H. Wu, F. Cai, R. Si, J. Xiao, S. Miao, S. Xie, F. Yang, Y. Li, G. Wang, X. Bao, Coordinatively unsaturated nickel–nitrogen sites towards selective and high-rate CO_2 electroreduction, Energy Environ. Sci. 11 (5) (2018) 1204–1210.
[17] F. Pan, B. Li, E. Sarnello, S. Hwang, Y. Gang, X. Feng, X. Xiang, N.M. Adli, T. Li, D. Su, G. Wu, G. Wang, Y. Li, Boosting CO_2 reduction on Fe-N-C with sulfur incorporation: synergistic electronic and structural engineering, Nano Energy 68 (2020) 104384.
[18] C. Jia, X. Tan, Y. Zhao, W. Ren, Y. Li, Z. Su, S.C. Smith, C. Zhao, Sulfur-dopant-promoted electroreduction of CO_2 over coordinatively unsaturated Ni-N_2 moieties, Angew Chem Int Ed Engl 60 (43) (2021) 23342–23348.
[19] Q. Li, W. Chen, H. Xiao, Y. Gong, Z. Li, L. Zheng, X. Zheng, W. Yan, W.C. Cheong, R. Shen, N. Fu, L. Gu, Z. Zhuang, C. Chen, D. Wang, Q. Peng, J. Li, Y. Li, Fe isolated single atoms on S N codoped carbon by copolymer pyrolysis strategy for highly efficient oxygen reduction reaction, Adv. Mater. 30 (2018) 1800588.
[20] X. Sun, Y. Tuo, C. Ye, C. Chen, Q. Lu, G. Li, P. Jiang, S. Chen, P. Zhu, M. Ma, J. Zhang, J.H. Bitter, D. Wang, Y. Li, Phosphorus Induced Electron Localization of Single Iron Sites for Boosted CO_2 Electroreduction Reaction, Angew Chem Int Ed Engl 60 (44) (2021) 23614–23618.
[21] S.-G. Han, D.-D. Ma, S.-H. Zhou, K. Zhang, W.-B. Wei, Y. Du, X.-T. Wu, Q. Xu, R. Zou, Q.-L. Zhu, Fluorine-tuned single-atom catalysts with dense surface Ni-N_4 sites on ultrathin carbon nanosheets for efficient CO_2 electroreduction, Appl. Catal. B 283 (2021) 119591.
[22] G. Kresse, J. Furthmüller, Efficiency of ab-initio total energy calculations for metals and semiconductors using a plane-wave basis set, Comput. Mater. Sci. 6 (1) (1996) 15–50.
[23] J.P. Perdew, K. Burke, M. Ernzerhof, Generalized gradient approximation made simple, Phys. Rev. Lett. 77 (18) (1996) 3865–3868.
[24] G. Kresse, D. Joubert, From ultrasoft pseudopotentials to the projector augmented-wave method, Phys Rev B 59 (3) (1999) 1758–1775.
[25] S.N. Steinmann, C. Corminboeuf, A system-dependent density-based dispersion correction, J Chem Theory Comput 6 (7) (2010) 1990–2001.
[26] H. Jin, X. Zhao, L. Liang, P. Ji, B. Liu, C. Hu, D. He, S. Mu, Sulfate ions induced concave porous S-N Co-doped carbon confined FeCx nanoclusters with Fe-N_4 sites for efficient oxygen reduction in alkaline and acid media, Small 17 (29) (2021) e2101001.
[27] B. Fang, Y. Xing, A. Bonakdarpour, S. Zhang, D.P. Wilkinson, Hierarchical CuO–TiO_2 hollow microspheres for highly efficient photodriven reduction of CO_2 to CH_4, ACS Sustainable Chem. Eng. 3 (10) (2015) 2381–2388.
[28] B. Fang, A. Bonakdarpour, K. Reilly, Y. Xing, F. Taghipour, D.P. Wilkinson, Large-scale synthesis of TiO_2 microspheres with hierarchical nanostructure for highly efficient photodriven reduction of CO_2 to CH_4, ACS Appl Mater Interfaces 6 (17) (2014) 15488–15498.
[29] Y. Wang, X. Cui, J. Zhao, G. Jia, L. Gu, Q. Zhang, L. Meng, Z. Shi, L. Zheng, C. Wang, Z. Zhang, W. Zheng, Rational design of Fe–N/C hybrid for enhanced nitrogen reduction electrocatalysis under ambient conditions in aqueous solution, ACS Catal. 9 (1) (2019) 336–344.
[30] J. Bai, B. Xi, H. Mao, Y. Lin, X. Ma, J. Feng, S. Xiong, One-Step Construction of N, P-codoped porous carbon sheets/CoP hybrids with enhanced lithium and potassium storage, Adv Mater 30 (35) (2018) e1802310.
[31] Y. Goto, K. Taniguchi, T. Omata, S. Otsuka-Yao-Matsuo, N. Ohashi, S. Ueda, H. Yoshikawa, Y. Yamashita, H. Oohashi, K. Kobayashi, Formation of Ni_3C nanocrystals by thermolysis of nickel acetylacetonate in oleylamine: characterization using hard X-ray photoelectron spectroscopy, Chem. Mater. 20 (2008) 4156–4160.
[32] F. Petraki, V. Papaefthimiou, S. Kennou, The electronic structure of Ni-phthalocyanine/metal interfaces studied by X-ray and ultraviolet photoelectron spectroscopy, Org. Electron. 8 (5) (2007) 522–528.
[33] Y. Hou, M. Qiu, M.G. Kim, P. Liu, G. Nam, T. Zhang, X. Zhuang, B. Yang, J. Cho, M. Chen, C. Yuan, L. Lei, X. Feng, Atomically dispersed nickel-nitrogen-sulfur species anchored on porous carbon nanosheets for efficient water oxidation, Nat Commun 10 (2019) 1392.
[34] F. Pan, B. Li, W. Deng, Z. Du, Y. Gang, G. Wang, Y. Li, Promoting electrocatalytic CO_2 reduction on nitrogen-doped carbon with sulfur addition, Appl. Catal. B 252 (2019) 240–249.
[35] Y. Ito, W. Cong, T. Fujita, Z. Tang, M. Chen, High catalytic activity of nitrogen and sulfur co-doped nanoporous graphene in the hydrogen evolution reaction, Angew Chem Int Ed Engl 54 (7) (2015) 2131–2136.
[36] Z. Yang, Z. Yao, G. Li, G. Fang, H. Nie, Z. Liu, X. Zhou, Xi'an Chen, S. Huang, Sulfur-doped graphene as an efficient metal-free cathode catalyst for oxygen reduction, ACS Nano 6 (1) (2012) 205–211.
[37] Y. Hou, M. Qiu, T. Zhang, J.i. Ma, S. Liu, X. Zhuang, C. Yuan, X. Feng, Efficient electrochemical and photoelectrochemical water splitting by a 3D nanostructured carbon supported on flexible exfoliated graphene foil, Adv Mater 29 (3) (2017) 1604480.
[38] S. Jiang, M. Chen, X. Wang, Y. Zhang, C. Huang, Y. Zhang, Y. Wang, Honeycomb-like nitrogen and sulfur dual-doped hierarchical porous biomass carbon bifunctional interlayer for advanced lithium-sulfur batteries, Chem. Eng. J. 355 (2019) 478–486.
[39] X. Wang, Y.u. Wang, X. Sang, W. Zheng, S. Zhang, L. Shuai, B. Yang, Z. Li, J. Chen, L. Lei, N.M. Adli, M.K.H. Leung, M. Qiu, G. Wu, Y. Hou, Dynamic activation of adsorbed intermediates via axial traction for the promoted electrochemical CO_2 reduction, Angew Chem Int Ed Engl 60 (8) (2021) 4192–4198.
[40] M. Huang, B. Deng, X. Zhao, Z. Zhang, F. Li, K. Li, Z. Cui, L. Kong, J. Lu, F. Dong, L. Zhang, P. Chen, Template-sacrificing synthesis of well-defined asymmetrically coordinated single-atom catalysts for highly efficient CO_2 electrocatalytic reduction, ACS Nano 16 (2) (2022) 2110–2119.
[41] H.B. Yang, S.-F. Hung, S. Liu, K. Yuan, S. Miao, L. Zhang, X. Huang, H.-Y. Wang, W. Cai, R. Chen, J. Gao, X. Yang, W. Chen, Y. Huang, H.M. Chen, C.M. Li, T. Zhang, B. Liu, Atomically dispersed Ni(i) as the active site for electrochemical CO_2 reduction, Nature, Energy 3 (2) (2018) 140–147.
[42] Q. Jia, N. Ramaswamy, H. Hafiz, U. Tylus, K. Strickland, G. Wu, B. Barbiellini, A. Bansil, E.F. Holby, P. Zelenay, S. Mukerjee, Experimental observation of redox-induced Fe–N switching behavior as a determinant role for oxygen reduction activity, ACS Nano 9 (12) (2015) 12496–12505.
[43] M. Gattrell, N. Gupta, A. Co, A review of the aqueous electrochemical reduction of CO_2 to hydrocarbons at copper, J. Electroanal. Chem. 594 (1) (2006) 1–19.